PAPER

Check for updates

Nanostructured electroless Ni deposited SnO_2 for solar hydrogen production†

Priyanka N. Birla, [ID] [a] Sudhir Arbuj, [ID] [a] Ratna Chauhan,[b] Manish Shinde, [ID] [a] Sunit Rane,[a] Suresh Gosavi [ID] [b] and Bharat Kale [ID] *[a,c]

Herein, Ni-decorated SnO_2 (Ni@SnO_2) nanostructures have been synthesized using SnO_2 as a matrix *via* a simple electroless deposition method for the generation of hydrogen, a potent near-future fuel. XRD analysis confirmed the generation of rutile SnO_2 in Ni@SnO_2. FESEM and FETEM imaging exhibited the formation of SnO_2 nanoparticles with a size of 10–50 nm, which are deposited with Ni nanoparticles (5–7 nm) and intermittent films (thickness 1–2 nm). The associated EDS elemental mapping validated Ni deposition on the surface of the SnO_2 nanoparticles, further supplemented by FTIR, Raman and XPS analysis. Slight red shifts in the band gaps of the Ni@SnO_2 nanostructures (in the range of 3.53–3.65 eV) compared to the pristine SnO_2 nanoparticles (3.72 eV) were observed. Also, intensity quenching of the band gap and associated defect peaks were observed in PL analysis. The Ni@SnO_2 nanostructures were used as photocatalysts and exhibited proficient hydrogen evolution. Among the samples, the 0.3 wt% Ni@SnO_2 nanostructures showed the greatest hydrogen evolution, *i.e.*, ~50 μmol g^{-1} h^{-1} under visible light irradiation *versus* pristine SnO_2 (8.5 μmol g^{-1} h^{-1}) owing to the enhanced density of active sites and effective charge separation. It is noteworthy that the hydrogen evolution is much better as compared to earlier reports of Pt-doped-SnO_2 based materials.

Introduction

Fuels play a vital role in the progressive industrialized economy, in which an enormous amount of energy is required for various processes such as heating, lighting, transportation, power generation, production, *etc*. Until the last few decades, the world relied heavily on fossil fuels. In the contemporary scenario, depletion of perishable energy sources as well as environmental issues such as global warming have arisen, and the world is facing an energy crisis that requires significant attention. Researchers are focusing on environmentally friendly concrete technologies for energy generation using various sustainable sources with assured energy security.

When the various sustainable energy fuel options are scrutinized, hydrogen is found to be the apt alternative, although it is in its infancy in terms of development of the technology (hydrogen economy) owing to the bottlenecks related to its safe and efficient storage and delivery.[1] Its vast energy capacity, as well as its relatively clean and energy-efficient nature, make hydrogen a proficient energy carrier.[2] As 8% of overall energy demand is predicted to be fulfilled *via* hydrogen by the year 2050, a need for the development of hydrogen production methods with near-zero greenhouse gas emissions has arisen.[3]

At present, the overall demand of hydrogen is overwhelmingly (>95% of total demand) satisfied by the steam reforming process or the partial oxidation of hydrocarbons with the inevitable generation of carbon dioxide.[4] As an alternative, water splitting is a relatively greener method of hydrogen production carried out using techniques such as thermochemical,[5] photo-fermentative,[3] and photo-electrolytical[6] methods *via* exposure to thermal, photo- or photo-electrical radiation. However, these techniques are either slow or energy intensive. One technology for H_2 production is photocatalytic water splitting; it entails photonic energy, which is considered to be the most abundant energy resource on Earth.[7]

In this context, the most suitable water splitting methodology is based on catalysts known as semiconductor photocatalysts that are activated under electromagnetic (solar) radiation, which split the water molecule into hydrogen and oxygen through the process known as photocatalysis.[1,8] Such photocatalytic water splitting leads to H_2 evolution on the photocatalyst surface *via* its interplay with water molecules, culminating in the generation of strong oxidizing mediators

[a]Centre for Materials for Electronics Technology, Off Pashan Road, Panchwati, Pune-411008, India. E-mail: bbkale1@gmail.com
[b]Department of Environment Science, Savitribai Phule Pune University, Pune-411007, India
[c]Material Science Department, MITWPU, University Paud Road, Pune 38, India
†Electronic supplementary information (ESI) available. See DOI: https://doi.org/10.1039/d4nr01194e

such as hydroxyl and superoxide radicals sans any costly or advanced reaction set-up.[9]

Considering the importance of photocatalytic water splitting, various types of photocatalysts and their combinations need to be reviewed for evaluation of their pros and cons. To date, numerous photocatalysts have been employed for hydrogen production, such as widely used conventional semiconductor metal oxides like TiO_2[10] and ZnO,[11] as well as other materials including WO_3,[12] $BiVO_4$,[13,14] BiOBr,[15] Bi_2WO_6,[16] Ag_2S,[17] Ag_3PO_4,[18] AgBr,[19] Ag_3VO_4,[20] CdS,[21] P/YPO_4,[22] metal–organic frameworks (MOFs),[23] SnO_2,[24] etc. Among these materials, tin dioxide (SnO_2), which has several polymorphs, is an earth-abundant, non-toxic, and chemically stable n-type semiconductor material with a wide direct band gap (3.6 eV), reasonable optical transparency, and significant electron mobility; therefore, it has been extensively exploited in sensors, solar cells, supercapacitors, Li-ion lithium batteries and photocatalysis.[25] However, as a photocatalyst, it suffers from its wide band gap, which impedes its response to visible light, and its notorious photogenerated charge carrier recombination; these have resulted in there being a relatively small number of reports on SnO_2-based photocatalytic water splitting studies.[26]

These intrinsic downsides can be overcome by implementing strategies such as band gap engineering, enhanced charge-carrier separation, and transmission and swift redox reaction through surface modification via exhaustive tactics including composite photocatalyst construction and tuning of the material preparation protocols for morphology control, which have been adopted to design novel SnO_2-based photocatalysts.[24,27,28] Various SnO_2-based composite photocatalyst preparation techniques, namely, hydro/solvothermal,[29] co-precipitation,[30] sol–gel,[31] polyol,[32] auto-combustion[33] and microwave methods,[34] among others, have been reported. Among these methods, co-precipitation synthesis exhibits benefits, including low-temperature processing, improved safety, economic advantages, and facilitated mass production.[35] SnO_2 composite formation can be achieved through the introduction of a metal/nonmetal combination for appropriate surface modification.[36] In this direction, co-catalyst-based semiconductor composite photocatalytic systems such as $Pt@SnO_2$,[37,38] $SnO_2/Pt/In_2O_3$,[39] $Pt@SnO_2$/graphene,[40] $Pt/SnO_2/GNs$,[41] $TiO_2/Pt/SnO_2$,[42] and $Au/Pt/SnO_2$[43] have been reported for photocatalytic applications. However, such noble-metal-based photocatalytic materials can prove to be costly, hampering their industrial applicability. Simultaneously, the need to reduce environmental pollution and the photocatalyst production process cost also need to be taken into account.[24]

Nickel has been recognized as a strong substitute for noble metal co-catalysts owing to its renowned catalytic behaviour in numerous chemical reactions in industry. In this context, Ni and NiO have been loaded over the surface of SnO_2 to enhance their properties.[26,35] For $Ni@SnO_2$ nanostructures, various synthesis techniques, such as chemical reduction,[44] solvothermal treatment,[35] photoreduction,[45] and wet and chemical reduction,[44] have been studied by researchers. It is worth noting that electroless plating, although typically executed for various metal-based surface microlayer coatings on workpieces, has surprisingly arisen as a substitute for constructing surface-loaded nano-assemblies of different materials.[46] It is an autocatalytic surface coating process in which the metal to be deposited on the surface of the nanomaterials can be used in a cost-effective manner due to the low concentration requirements, control of the phase and morphology formation for large surface areas, etc., and has become a trending theme in the nano-assembly of metal-loaded semiconductor composites.[47,48] This technique, which is also known as electroless loading, is mouldable with respect to the substrates being metallized and can deposit metallic nanoparticles or films on materials in the solid, liquid or gaseous states with different chemical forms, sizes and shapes.[49] It can generate nanoparticles having varied morphologies such as nanotubes, nanoparticles, nanowires, and ultrathin films, etc., on the surface of the host materials by using a simple solution chemistry approach.[50] To the best of our knowledge, electroless Ni loading over the surface of an SnO_2 nanostructure has not been reported so far.

In this context, $Ni@SnO_2$ nanostructure photocatalysts have been prepared via the coprecipitation of SnO_2 nanoparticles followed by Ni loading using the electroless plating technique. The study of the effect of Ni loading over the surface of the SnO_2 nanoparticles and their photocatalytic water splitting leading to hydrogen production has been accomplished. The overall results established the efficacy of hydrogen production, revealing its utility as a scalable and cost-effective technique.

Materials and methods

Materials

For synthesis of the SnO_2 nanopowders, the required precursors, namely, stannous chloride dihydrate ($SnCl_2 \cdot 2H_2O$), methanol, and NH_4OH, were procured from Qualigens and SRL, India, respectively. Electroless nickel loading was performed using a commercial electrochemical bath that was procured from Grauer & Weil (India) Limited, which was composed of various solutions for cleaning, mild etching, pre-activation, activation and finally Ni loading. For the acid wash after the mild etching step, H_2SO_4 (98% conc., SRL chemicals, India) was diluted with deionized water to prepare a 10% sulphuric acid solution.

Material preparation

Synthesis of SnO_2 nanopowders. A facile co-precipitation method was employed for the preparation of the SnO_2 nanopowders. In this process, 0.1 M stannous chloride dihydrate ($SnCl_2 \cdot 2H_2O$) was dissolved in a 4 : 1 v/v MeOH : distilled water mixture. Upon complete dissolution, liquor ammonia was added to obtain a pH of 8, leading to the formation of an off-white coloured precipitate, which was washed with distilled water until neutralization under centrifugation, dried and then

calcined at 650 °C for 6 h and used as-is for further characterization and Ni loading.

Autocatalytic Ni deposition on the SnO₂ nanopowder surface. The details of Ni bath preparation process were provided in our previous work.[48] The electroless nickel loading process entailed a number of steps as detailed in Table T1 (ESI†) with continuous stirring. Centrifugation was carried out at the conclusion of each step. Fig. 1 shows all of the procedures involved collectively in the synthesis of SnO₂ nanoparticles and autocatalytic deposition of nickel on their surfaces. The SnO₂ nanoparticle surfaces were normally cleaned in three steps; using a cleaning solution that was kept at 60 °C for 10 min, followed by treatment with mild etching and acid solutions for 4 and 2 min, respectively, and centrifugation was carried out after each stage was finished with a water wash. After cleaning, the surface of the SnO₂ nanopowder was treated with a pre-activator solution for 2 min. However, after this step, there was no water rinsing.

By exposing the preactivated SnO₂ nanoparticles to activator and post-activator solutions for 5 min each, followed by rinsing them with water, the powder became surface activated. The surface-activated SnO₂ nanopowder was then exposed to Ni loading for 15 min by placing it in a Ni bath that was kept at a pH of 5.2 and a temperature of 85–90 °C (Fig. 1). The surface-activated SnO₂ nanoparticles were subjected to electroless Ni baths at different concentrations to adjust the Ni wt.% loading. The resulting samples were then utilized for photocatalytic water splitting (Table 1).

Characterization techniques

Crystalline behaviour study of the Ni@SnO₂ nanostructures was accomplished using powder X-ray diffraction (XRD, Rigaku MiniFlex 600, Cu-Kα1 radiation source of wavelength 1.54 Å) method. PHI Versa Probe XPS instrument employed for X-ray photoelectron spectroscopy (XPS) assisted the elemental compositional analysis of the pristine SnO₂ and 0.3% Ni@SnO₂ samples. The inductively coupled plasma optical emission spectroscopy (ICP-OES) technique was employed to confirm

Table 1 Electroless Ni bath composition for variable Ni wt% loading over SnO₂ nanoparticles

Sr. no.	Sample code (Ni wt%)	Nickel salt solution (mL)	Reducing agent solution (mL)	Calculated % Ni loading concentration
1	Pristine SnO₂	0	0	0
2	0.1%Ni@SnO₂	0.2	0.374	0.1
3	0.2%Ni@SnO₂	0.4	0.748	0.2
4	0.3%Ni@SnO₂	0.6	1.112	0.3
5	0.4%Ni@SnO₂	0.8	1.496	0.4
6	0.5%Ni@SnO₂	1.0	1.870	0.5

the Ni concentration of the synthesized products using a Spectroblue, Amtek. For these measurements, a typical sample (200 mg) was digested (in conc. HNO₃ (4 mL) and 30% H₂O₂ (1 mL)) in a microwave, and then diluted to 50 mL. The resultant solution was filtered and run through the calibration curve. A Renishaw Invia Raman microscope equipped with a 532 nm laser was utilized to study the Raman spectra of the Pristine-SnO₂ and Ni@SnO₂ nanostructure samples. Room temperature diffuse reflectance UV-visible absorbance spectra (UV-DRS) of the prepared materials were obtained in the range of 200–800 nm using a PerkinElmer LAMBDA 950 UV-VIS-NIR spectrophotometer. Photoluminescence (PL) emission spectra of the as-synthesised nanostructures were obtained using a Shimadzu (RF5301PC) spectrofluorometer at an excitation wavelength of 350 nm.

An IRAffinity-1S 01130 Shimadzu spectrometer was exploited for measuring Fourier transform infrared (FTIR) spectra between 400 and 4000 cm⁻¹. Morphological and microstructural investigations were performed using field emission scanning electron microscopy (FESEM, FEI NOVA NANOSEM 450) and field emission transmission electron microscopy (FETEM by JEOL, JEM-2200FS). For typical FETEM analysis, the test sample was carefully prepared by dispersing the sample powder in ethanol and then drop-casting it onto a carbon-coated grid. To obtain high imaging and spatial resolution with chemical mapping of the material, scanning trans-
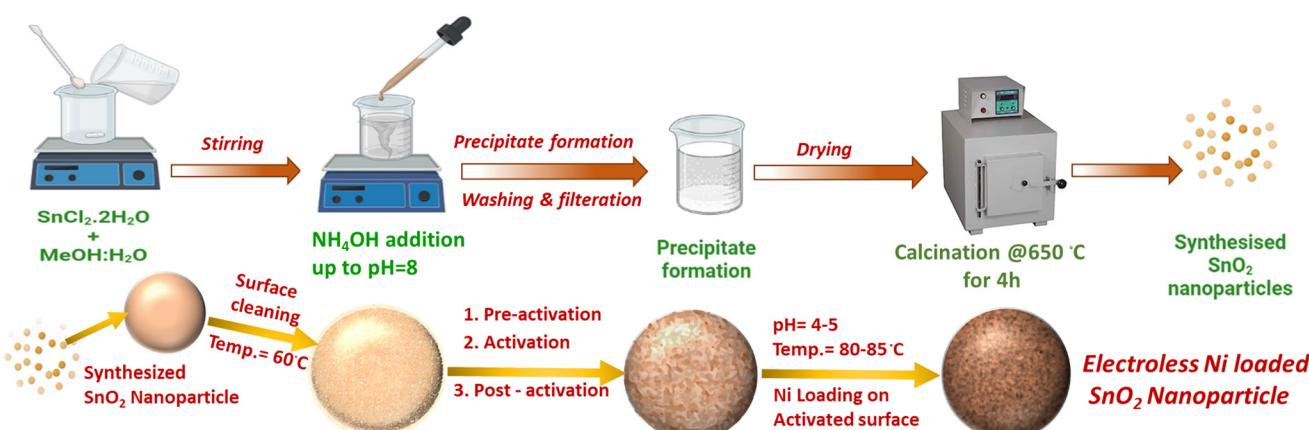
Fig. 1 Process schematic for the synthesis of SnO₂ nanoparticles and their electroless loading with Ni.

mission electron microscopy (STEM) in bright field (BF) mode equipped with energy dispersive X-ray spectroscopy (EDS) coupled elemental mapping using a JEOL JEM2200FS operated at 200 kV was employed. The samples' porosity and surface area were determined using Brunauer–Emmett–Teller analysis (BET: Quantachrome NOVA touch LX1).

Photocatalytic hydrogen generation

Photocatalytic hydrogen generation from water was accomplished using a photocatalytic reactor set-up consisting of a total 100 mL airtight cylindrical quartz photochemical reactor with an attached cooling jacket for water circulation. A solar simulator (CEL-NP2000) with AM 1.5 G illumination (100 mW cm^{-2}) and a hood fan to disperse surplus heat was the illumination source. A standard photocatalytic experiment involved dispersing 20 mg of the photocatalyst in 40 mL of an aqueous solution mixture containing 20% methanol (v/v). The 60 mL open space of the photoreactor was sealed with a rubber septum, and the catalyst was dispersed uniformly *via* ultra-sonication for 5 min. The resultant dispersion was purged with ultra-high purity (UHP-99.999%) nitrogen gas in order to eliminate dissolved oxygen from the solution and all the gases from the reactor's headspace. Gas chromatography (GC) with a thermal conductivity detector (Shimadzu GC-2014c; Ar carrier gas and molecular sieve-5 Å column) was employed for gas examination in the reactor's free space both before and after it was exposed to sunlight. At intervals of fifteen minutes, the reactor's hydrogen gas yield was measured by collecting the gas in the syringe and feeding it into the GC equipment.

Photoconductivity studies

A Keithley source meter (2450) was used for electrical measurement of pristine SnO_2 and $Ni@SnO_2$ nanostructure samples. A Class ABA Solar Simulator was used for white light illumination with a power density of 12 mW cm^{-2}.

Electrochemical studies

A CH 660C electrochemical analyzer (CH Instruments, Shanghai, China) with two electrodes was employed for the electrochemical impedance spectroscopy (EIS) study. Pt and the $Ni@SnO_2$ nanostructures played the roles of counter and working electrodes, respectively. Electrochemical impedance spectroscopy (EIS) with a 10 mV alternating signal was used to examine the electron transport parameters in the 10^{-2}–10^5 Hz frequency range.

Results and discussion

XRD

The phase purity and crystallinity of the as-synthesized pristine SnO_2 and $Ni@SnO_2$ nanostructures were established using X-ray diffraction, and the results are shown in Fig. 2. The prima-facie XRD reflections of the pristine SnO_2 and $Ni@SnO_2$ nanostructures show that the prepared materials were well matched with JCPDS number 41-1445 with the peaks exhibit-
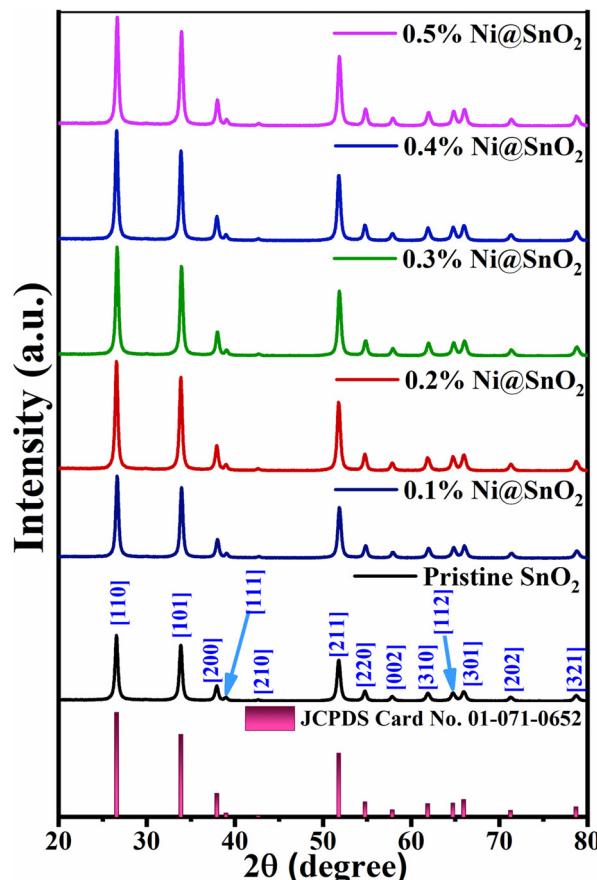

Fig. 2 X-ray diffractograms of the prepared pristine SnO_2 and $Ni@SnO_2$ nanostructure samples.

ing reasonable similitude with rutile-phase tetragonal SnO_2. The observed peaks at 2θ values of 26.57, 33.89, 37.90, 38.06, 51.79, 54.74, 57.92, 61.92, 64.76, 66.05, 71.36 and 78.79° were in good agreement with the corresponding crystalline [110], [101], [200], [111], [211], [220], [002], [310], [112], [301], [202] and [321] planes.[51,52]

The substantial broadening of peaks observed in all the samples is an indication of the nanoscale nature of all the samples.[53] Diffraction peaks due to Ni are not observed in any of the samples due to the low Ni loading percentage, which is lower than the detection limit of XRD, and probably due to formation of even smaller Ni nanoparticles/surface coatings on the SnO_2 nanoparticles.

X-ray photoelectron spectroscopy

Analysis of the surface chemical and electronic states of the pristine SnO_2 and $Ni@SnO_2$ nanostructure samples was carried out using the XPS technique (Fig. 3). The XPS survey spectra of both pristine SnO_2 and the 0.3%$Ni@SnO_2$ nanostructure sample revealed the presence of characteristic peaks due to the elements Sn and O, with an additional peak assigned to Ni in the 0.3%$Ni@SnO_2$ nanostructure sample (Fig. 3a). Further insights into the composition were obtained
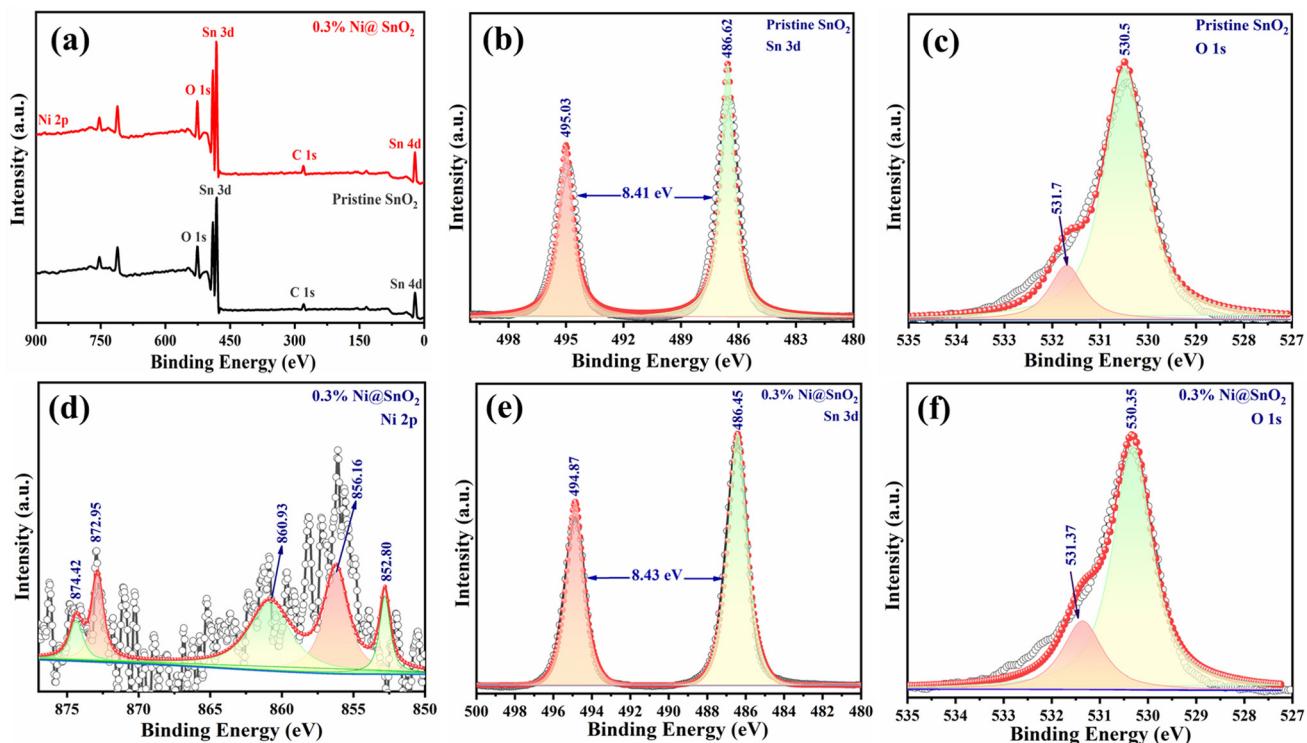
Fig. 3 XPS spectra of pristine SnO_2 and 0.3% Ni@SnO_2 nanostructure samples. (a) Survey scan for both samples, and deconvoluted high-resolution scans corresponding to the elements (b) Sn 3d and (c) O 1s for Pristine SnO_2 and (d) Ni 2p, (e) Sn 3d and (f) O 1s for the 0.3% Ni@SnO_2 nanostructure.

from the high-resolution scans for the respective elements. The high-resolution scans corresponding to Sn 3d (Fig. 3b and e) displayed splitting of peaks into doublets attributable to Sn $3d_{5/2}$ and Sn $3d_{3/2}$ with values of 486.62 eV and 495.03 eV and 486.45 eV and 494.87 eV for the pristine SnO_2 and 0.3% Ni@SnO_2 nanostructure sample, respectively.[54,55]

The O 1s peak was observed to be fragmented into an intense peak at 530.50 and 530.35 eV for pristine SnO_2 and 0.3%Ni@SnO_2 nanostructure samples respectively as shown in Fig. 3c and f, which could be assigned to O^{2-} bonded with Sn^{4+}. Another peak at 531.37 eV in both these samples could be ascribed to defect sites or vacancies.[55]

The high-resolution scan for Ni of the 0.3%Ni@SnO_2 nanostructure sample revealed multiple peaks (Fig. 3d). The presence of peaks at 872.95 eV and 856.16 eV were credited to Ni 2p splitting into Ni $2p_{1/2}$ and Ni $2p_{3/2}$ orbitals, respectively. The peaks at 860.93 and 874.42 eV are due to the presence of satellite peaks. The generation of zerovalent Ni (Ni^0) was confirmed by the existence of a peak at 852.8 eV attributable to the reduction of the Ni precursor during electroless loading process. Moreover, as a hydrogen adsorption site, the presence of Ni^0 should promote high activity.[56,57]

ICP-OES spectroscopy

Table 2 shows the ICP-OES analysis results for the Ni@SnO_2 nanostructures, demonstrating that the experimental wt.%

Table 2 ICP-OES composition results for Ni@SnO_2 nanostructure powders

Sr. No.	Ni weight % value	
	Calculated	Observed
1	0.1% Ni@SnO_2	0.102
2	0.2% Ni@SnO_2	0.190
3	0.3% Ni@SnO_2	0.294
4	0.4% Ni@SnO_2	0.409
5	0.5% Ni@SnO_2	0.492

loading of Ni was consistent with our theoretical calculations performed during the Ni loading studies.

Raman spectroscopy

Classically, rutile phase SnO_2 with a tetragonal structure gives rise to four basic Raman-active peaks centred at wavenumbers of 633, 755, 782 and 477 cm^{-1}, which are characteristically allocated to the A_{1g}, B_{1g}, B_{2g} and E_g modes respectively.[58,59] These modes were significantly observed in the pristine and Ni@SnO_2 samples (Fig. 4 and Table 3). Moreover, a few Raman-silent modes, such the forbidden modes A_{2g} and B_{1u} as well as the infrared active modes Eu (TO), Eu (LO) and A_{2u}, were also observed (Fig. 4b).[47,60,61]

The presence of IR-active modes in the Raman spectra could be associated with lattice imperfections and superficial
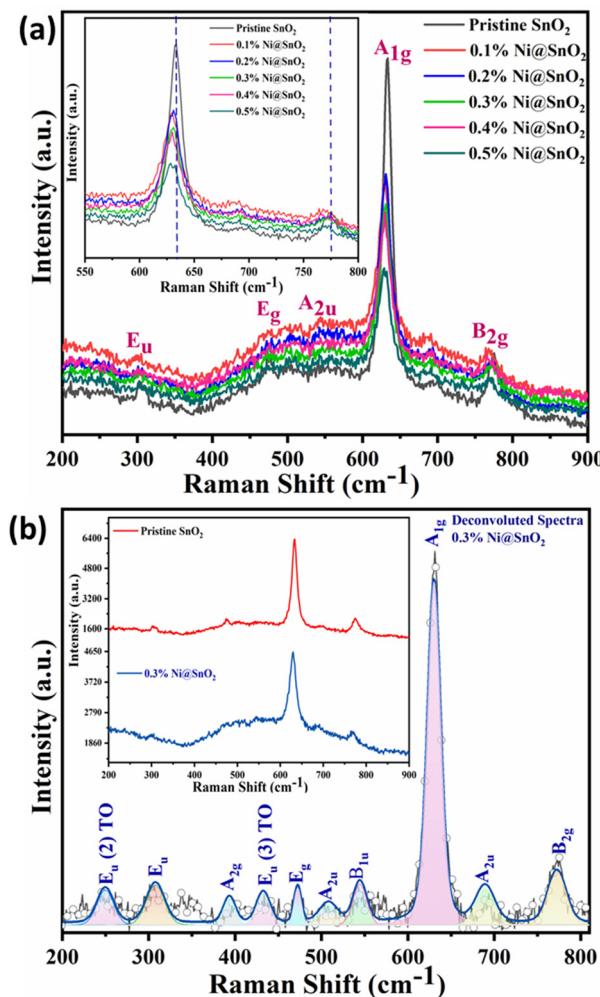
Fig. 4 Raman spectra of the prepared pristine SnO_2 and $Ni@SnO_2$ nanostructure in the (a) 200–900 cm^{-1} range (inset: 550–800 cm^{-1} range) and (b) spectra of 0.3%$Ni@SnO_2$ nanostructures (inset: 200–900 cm^{-1} range for pristine SnO_2 and 0.3%$Ni@SnO_2$ nanostructure).

Table 3 Reported vs. observed Raman vibrational modes of pristine SnO_2 and $Ni@SnO_2$ nanostructure samples

Sr. No.	Reported vibrational modes and their assignments[52,59–63] (cm^{-1})	Observed modes and their assignments (cm^{-1})
1	247.4 (E_u (2) TO)	249
2	306 (Eu)	308
3	392.8 (A_{2g} Silent)	392
4	430.4 ((E_u (3) LO), IR active)	432
5	472.9 (E_g)	472
6	506 (A_{2u}(TO), IR active)	507
7	544 (B_{1u})	544
8	631.6 (A_{1g})	631
9	691.7 (A_{2u})	689
10	774.2 (B_{2g})	773

defects primarily due to the nanoscale size of SnO_2. However, the intensity of peaks associated with the Raman-active modes were observed to decrease, while the intensity increased

for the IR-active peaks, owing to various processes during electroless loading of Ni on the SnO_2 nanoparticle surface. Such processes may lead to the generation of a non-stoichiometric [110] plane reconstructed SnO_x surface. Additionally, peaks due to both the Raman and IR active modes were observed to be shifted to slightly lower frequencies, which could be attributed to the presence of surface vacancies.[62]

UV-DRS spectroscopy

The bulk band gap (3.57 eV) of rutile-type SnO_2 is positioned at the C-point of its Brillouin zone, corresponding to the direct transition.[26] The optical properties of the Pristine-SnO_2 and $Ni@SnO_2$ nanostructures were evaluated using UV-DRS and Tauc plots (Fig. 5). The Pristine-SnO_2 sample exhibited a band gap of 3.72 eV, which is blue shifted relative to the bulk band gap owing to its nanosized nature, as seen from the FESEM and FETEM images. In the case of the $Ni@SnO_2$ nanostructures, the band gap values decreased slightly (bathochromic or red shift) upon increasing the Ni loading percentage from 0.1 to 0.5%, which may be attributable to the generation of defects and interaction between the d electrons of Ni^{2+} and the electrons obtained from O^{2-} and Sn^{4+}.[64,65]

Photoluminescence spectroscopy

The PL spectra of the pristine SnO_2 and $Ni@SnO_2$ nanostructures are shown in Fig. 6. At an excitation wavelength of 325 nm, all the samples exhibited two distinct broad emission bands, a higher intensity one around 364 nm (UV region) and another at 468 nm (visible region) having lower intensity. The presence of a peak at 364 nm (3.40 eV) could be attributed to the near-band-edge UV emission of the SnO_2 nanoparticles due to the radiative recombination of conduction band electrons and valence band holes. The visible region emission peak around 468 nm (2.65 eV) could be attributed to the non-radiative transition from defects such as interstitials and/or
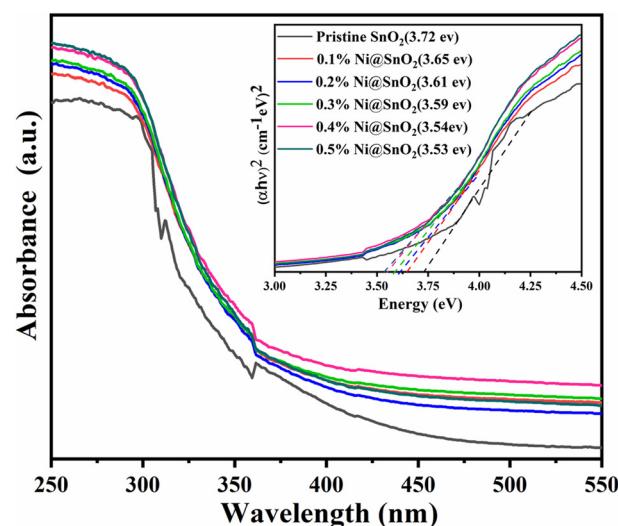
Fig. 5 UV-DRS spectra (inset: Tauc plot) of pristine-SnO_2 and $Ni@SnO_2$ nanostructures.
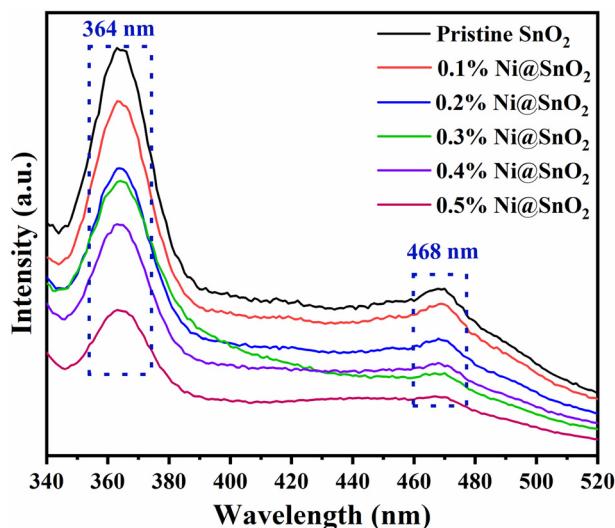
Fig. 6 PL spectra of pristine SnO$_2$ and Ni@SnO$_2$ nanostructures.

Fig. 7 FTIR spectrum of pristine SnO$_2$ and 0.1 to 0.5% Ni@SnO$_2$ nanostructures.

vacancies forming inter-band trapped states.[66] When Ni was loaded on the SnO$_2$ nanoparticle surfaces, although similar PL signatures were observed for all the samples owing to the analogous lattice structure, an appreciable change in the intensity ratios of the peaks in the UV and visible regions could be noted.[66] The intensity of the peak around 364 nm gradually decreased with increasing the Ni loading from 0.1 to 0.5%, as penetration of light was hindered. Although a reduction in the intensity of the peak at around 468 nm was also observed, this reduction was most pronounced for 0.3% Ni@SnO$_2$ nanostructure sample. Thus, the Ni loading became a significant parameter as PL peak intensity suppressor *via* the generation of a non-radiative epicentre thwarting excessive e$^-$/h$^+$ pair recombination.[48] These effects aid not only in effective charge separation, but also in carrier mobility improvement.[67]

FTIR spectroscopy

Fig. 7 presents the FTIR spectrum of pristine SnO$_2$ and the 0.1 to 0.5% Ni@SnO$_2$ nanostructures. FTIR analysis was carried out to examine the existence of functional groups and the vibrational stretching of chemical bonds. Usually, peaks below 1000 cm^{-1} correlate with metal oxide bonds, and our samples exhibited analogous results.[68] A notable broad band in the 700–400 cm^{-1} region is linked with the stretching modes of the vibrations of crossed-over bonds between Sn–O–Sn and Ni–Sn–O, indicating the formation of Ni-decorated SnO$_2$ nanostructures.[69,70]

FESEM imaging

The surface morphologies of the prepared samples were examined using field emission scanning electron microscopy (FESEM) as shown in Fig. 8. The low-magnification images (Fig. 8a, c, e, g, i and k) corresponding to the as-synthesized SnO$_2$ and Ni@SnO$_2$ powders prepared with varying composition showed the formation of brick-like micron-sized agglom-erated morphologies. The FESEM images of the as-synthesized SnO$_2$ and Ni@SnO$_2$ nanopowders at low magnification revealed spherical, rod-like, and irregular faceted nanoscale morphologies having sizes in the range of 30–60 nm (Fig. 8b, d, f, h, j, and l). In the Ni@SnO$_2$ nanopowders, the morphologies of the SnO$_2$ nanoparticles are not pronounced, which might be due to Ni nanoparticle loading/capping on their surfaces. However, Ni nanoparticles could not be distinctly observed in the FESEM images, probably due to their tiny size and capping.
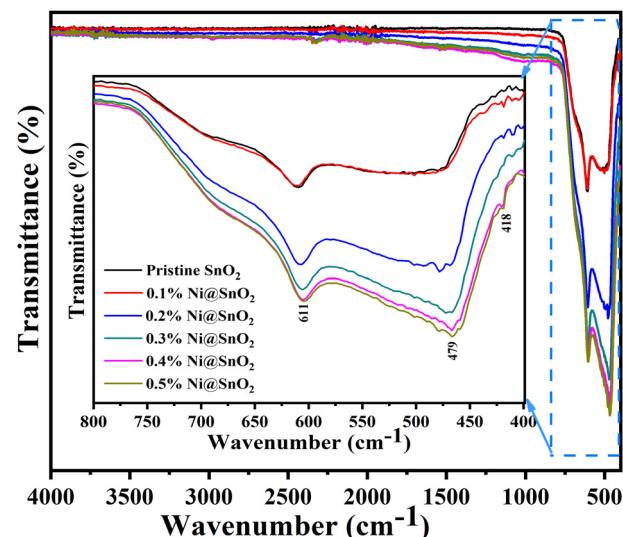
FETEM imaging

FETEM images of 0.3%Ni@SnO$_2$ nanostructures are shown in Fig. 9. The low-magnification image divulged the formation of nanoparticles in the size range of 10–50 nm (Fig. 9a). The intermediate-magnification images presented in Fig. 9b and c revealed that the nanoparticles have spherical, irregular, hexagonal and faceted rod-like morphologies. Additionally, a few nanoparticles having sizes of 5–7 nm were also observed. The lattice images depicted in Fig. 9d and e reveal two important features of Ni loading. Ni was found to partially overlay the SnO$_2$ nanoparticle surfaces with a thickness of 1–2 nm and length of 50–60 nm (Fig. 9d). Additionally, the formation of Ni nanoparticles with a size of 5–7 nm over the SnO$_2$ nanoparticle surfaces was also observed (Fig. 9e). The coating/formation of Ni nanoparticles was confirmed by matching the lattice spacing values of these coating/nanoparticles with JCPDS *d*-values corresponding to the (111) and (200) planes of Ni.[52]

High-resolution TEM images corresponding to 0.3% Ni@SnO$_2$ nanostructures (Fig. 9d and e) disclosed the significantly crystalline nature of the generated SnO$_2$ nanoparticles, most of them possessing a single-phase nature with different lattice orientations, as revealed from *d*-spacings of 3.26, 2.64 and 1.49 Å assigned to the (110), (101) and (310) planes,
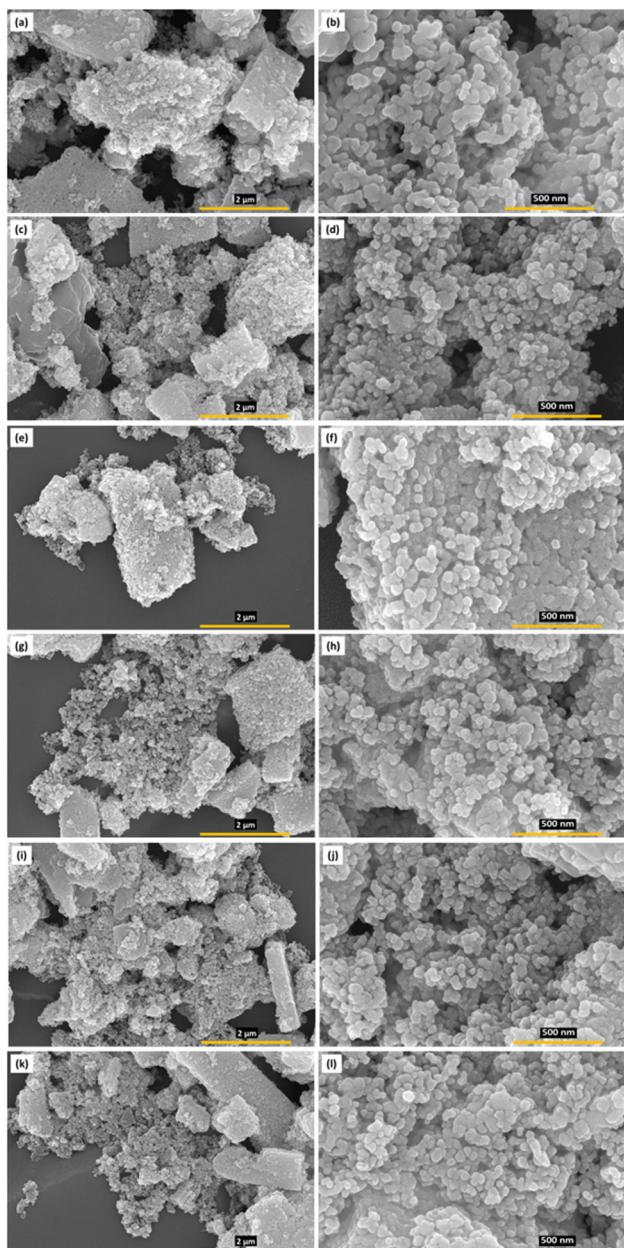
Fig. 8 FESEM images of pristine SnO$_2$ (a and b) and 0.1 to 0.5% Ni@SnO$_2$ nanostructure powders corresponding to Ni loadings of (c and d) 0.1, (e and f) 0.2, (g and h) 0.3, (i and j) 0.4, and (k and l) 0.5% at low and high magnifications, respectively.

respectively. Thus, FETEM analysis supports the symbiotic manifestation of Ni on the SnO$_2$ surface.[71]

The corresponding SAED pattern (Fig. 9f) revealed the nanocrystalline nature of the 0.3%Ni@SnO$_2$ nanostructure, observed as regular spots in the rings. Further, intermittent diffraction rings in SAED pattern matching the (110), (101), (201), (211), (220) planes evince SnO$_2$ nanoparticles as the major contributor to the crystalline phase in the sample. The absence of nickel-related phases corroborated the XRD analysis. However, although high-resolution lattice imaging con-

firmed the presence of Ni nanoparticles, they could not be observed via either XRD or SAED due to their relatively small size and lower concentration.[72]

EDS analysis equipped with elemental mapping was employed to evaluate the compositions of oxygen, tin and nickel, which matched approximately to the elements in 0.3% Ni@SnO$_2$ nanostructure as per the stoichiometry (Fig. 10a and b). Additionally, the elemental mapping images corresponding to these elements revealed that Ni was uniformly deposited over the SnO$_2$ surface (Fig. 10c, d and e).[72]

BET surface area analysis

The results pertaining to BET surface area analysis of pristine SnO$_2$ as well as the Ni@SnO$_2$ nanostructures with respect to nitrogen adsorption and desorption isotherms, BJH pore size, etc., are presented in Fig. 11 and Table 4. Nitrogen adsorption–desorption isotherms of type IV with H3 category hysteresis loops were observed for the as-synthesized pristine and nano-structure samples.[73] The surface area was calculated to be 9.9 m^2 g^{-1} with a pore diameter of 1.8820 nm for the pristine SnO$_2$ sample. As the Ni loading was increased to 0.3%, the surface area was found to increase gradually to 19.6 m^2 g^{-1} with a corresponding reduction in the pore diameter to 1.6769 nm, which might be due to the generation of tiny Ni nanoparticles as observed in the FETEM images. Further increasing the Ni loading led to a gradual decrease in the surface area due to excessive Ni nanoparticle loading, which filled the pores.[74]

Photoelectrochemical study

Nyquist plot analysis furnishes a wide-ranging understanding of the interactions among charge transfer kinetics, recombination processes, and catalytic activity in defining the efficacy of hydrogen generation in photoelectrochemical systems. The typical plot is presented as a semicircle of a complex impedance plane, with superior potency indicated by a smaller semicircle at higher frequencies, which signifies fast charge transfer and a lower rate of recombination.[75]

Pristine SnO$_2$ exhibited the largest semicircle, with an electrochemical reaction resistance (R_{ct}) of 130 Ω, while the lowest value of 65 Ω was observed for the 0.3%Ni@SnO$_2$ composite (Fig. 12). The distinctly superior electrochemical performance observed in the Nyquist plot for 0.3% Ni@SnO$_2$ compared with lower and higher Ni loading concentrations accentuates its potential as a propitious contender for photoelectrochemical hydrogen production applications (Fig. 12).

Faster charge transfer kinetics at the electrode–electrolyte interface were demonstrated via the smaller semicircle in the Nyquist plot for 0.3% Ni@SnO$_2$, which enables efficient conversion of photoexcited electrons to hydrogen ions, leading to higher hydrogen evolution rates. At lower Ni@SnO$_2$ composite surface deposition concentrations, the insufficient loading levels lead to slower charge transfer kinetics, whereas at higher loading concentrations of Ni, increased surface deposition
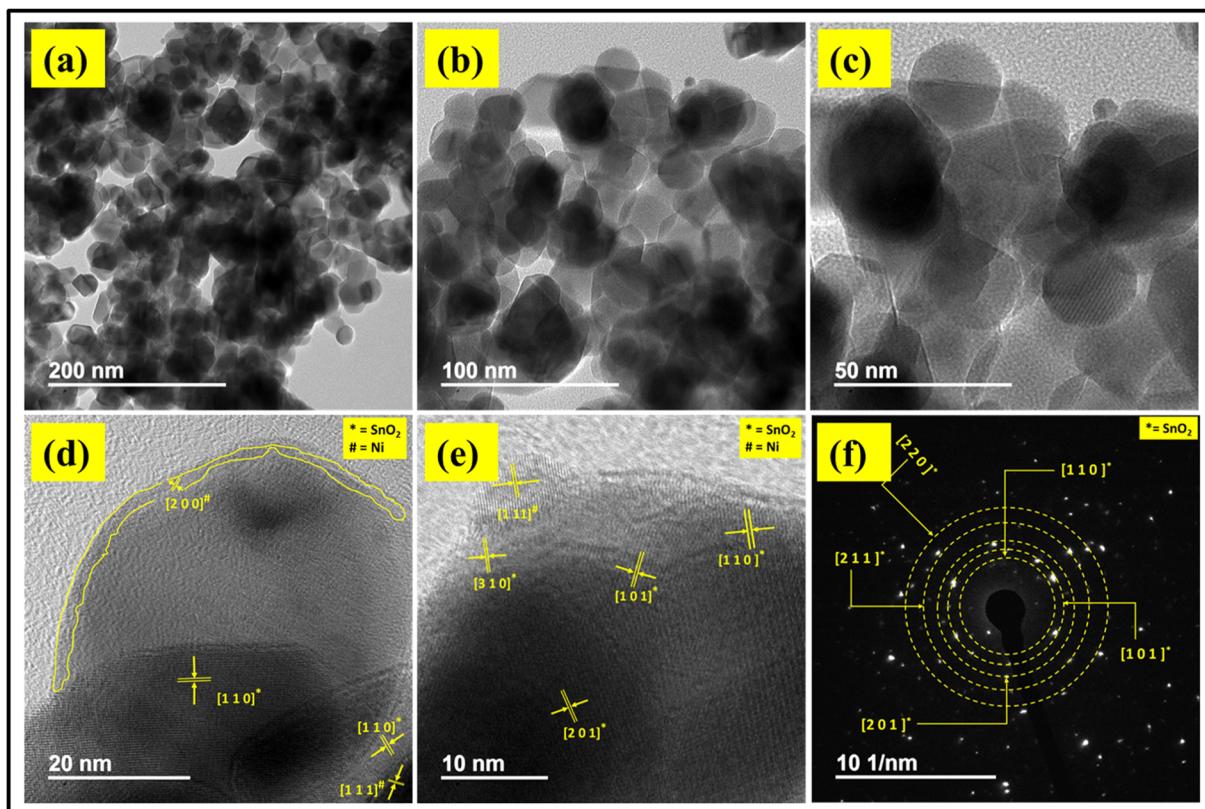
Fig. 9 FETEM images of 0.3% Ni@SnO$_2$ nanostructures at low magnification (a); their HRTEM images (b), (c), (d) and (e); and the corresponding SAED patterns (f).
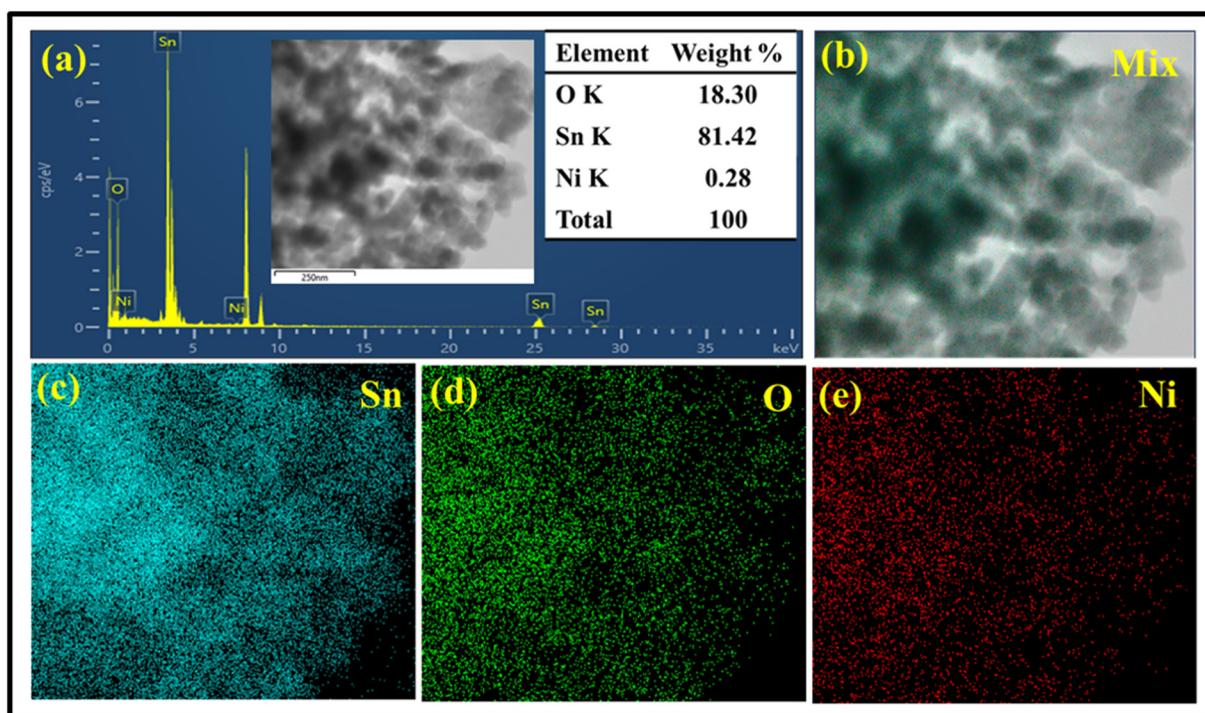

Fig. 10 FETEM-EDS-elemental mapping images of 0.3% Ni@SnO$_2$ nanostructures. (a) EDS graph and elemental mapping images: (b) mix, (c) Sn, (d) O and (e) Ni.
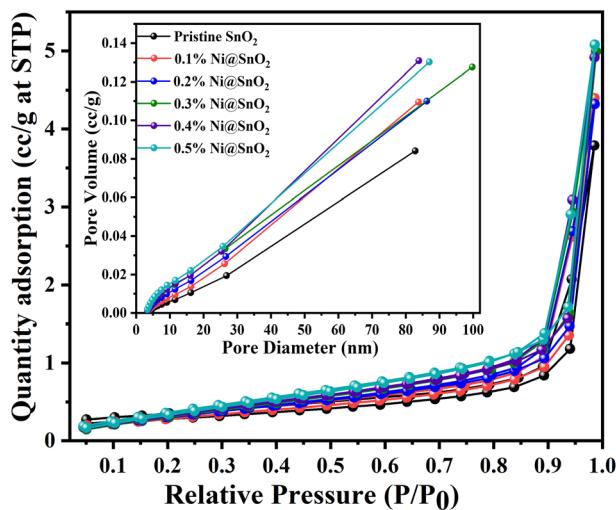
Fig. 11 BET surface area graphs corresponding to the relative pressure for pristine SnO_2 and Ni@SnO_2 nanostructures (inset: pore size distribution curve).

Table 4 BET surface area analysis of pristine SnO_2 and Ni@SnO_2 nanostructure samples

Sample	BET surface area (m^2 g^{-1})	Total pore volume (cm^3 g^{-1})	BJH pore size (nm)	H_2 generation (μmol g^{-1} h^{-1})
Pristine SnO_2	9.9	0.0872	1.8820	8.52
0.1% Ni@SnO_2	13.2	0.1139	1.6899	16.2
0.2% Ni@SnO_2	15.1	0.1266	1.6834	25.67
0.3% Ni@SnO_2	19.6	0.1316	1.6769	49.98
0.4% Ni@SnO_2	18.2	0.1346	1.6811	39.78
0.5% Ni@SnO_2	17.3	0.1351	1.6817	28.4
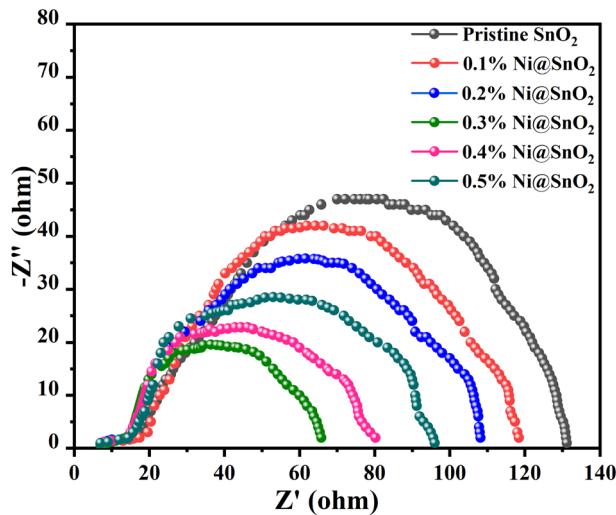
Fig. 12 Nyquist plot for SnO_2 and 0.1 to 0.5% Ni@SnO_2 nanostructures.

causes reorganization or electronic effects that hinder charge transfer; the optimum balance of both is achieved at 0.3% Ni loading.

Photoconductivity study

The *I–V* characteristics of pristine SnO_2 and 0.3% Ni@SnO_2 photodetectors with a voltage sweep of −10.0 V to 10.0 V are shown in Fig. 13a. The linear behaviour of all the *I–V* curves confirmed the generation of ohmic contact between the samples and the ITO electrodes. The observed photocurrents for the pristine SnO_2 and 0.3% Ni@SnO_2 photodetectors under the light illumination were 16.5 nA and 20.9 nA, respectively, compared to 10.91 nA for the same measurement in the dark for 0.3% Ni@SnO_2 photodetectors. The nickel loading on the SnO_2 surface effectively improved the charge transport, leading to an enhancement of the photocurrent. The photoresponse of the pristine SnO_2 and 0.3% Ni@SnO_2 based photodetectors at 0.5 V bias voltage is shown in Fig. 13(b) for five cycles. Both the pristine SnO_2 and 0.3% Ni@SnO_2 sample based photodetectors showed a swift response to light with a constant and stable current over several cycles. The rise times observed for the pristine SnO_2 and 0.3% Ni@SnO_2 photodetectors under light illumination and dark conditions were found to be 800, 600 and 1200 ms, with corresponding fall times of 1210, 1000 and 1800 ms, respectively. The presence of nanoscale Ni loading on the SnO_2 surfaces improves charge separation and introduces additional electrochemical reaction
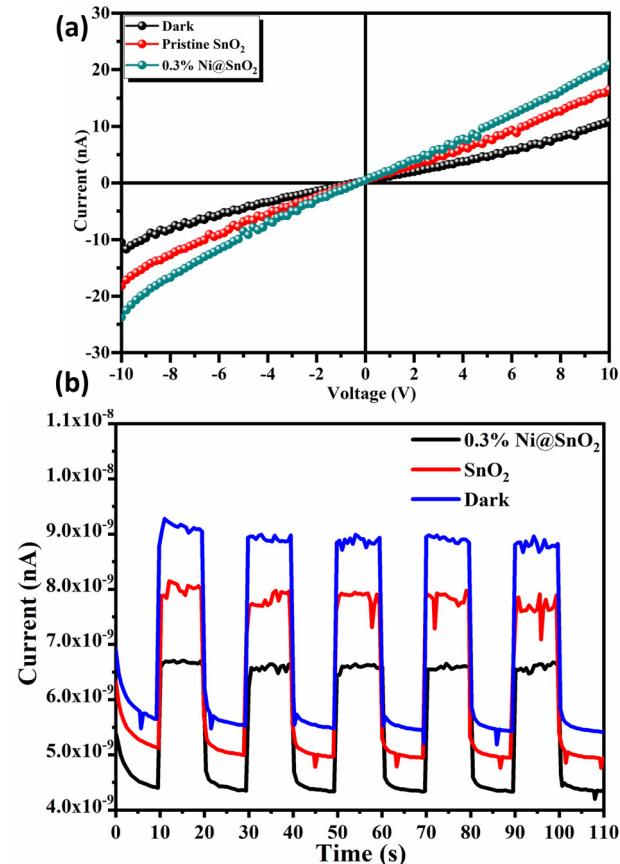

Fig. 13 (a) *I–V* characteristics and (b) photo-response of pristine SnO_2 and 0.3% Ni@SnO_2 photodetectors.

pathways or active sites, leading to an increase in the overall photocurrent response.

Cyclic voltammetry (CV) profiles of SnO_2 and 0.3% $Ni@SnO_2$ were obtained (Fig. 14) to further probe their photo-electrochemical behaviour. Although the CV profiles did not exhibit the rectangular shape typically associated with ideal capacitive behaviour, the increase in current observed for the 0.3%$Ni@SnO_2$ as compared to pristine SnO_2 indicated an enhancement in photoelectrochemical activity. The higher current in the 0.3%$Ni@SnO_2$ revealed the generation of a greater number of charge carriers and/or a more efficient charge transfer process, which could be directly correlated with an increase in charge storage capacity. Additionally, the larger area enclosed in the CV curves of 0.3%$Ni@SnO_2$ signi-fied higher capacitance, reflecting the material's ability to store and discharge more charge carriers.

Photocatalytic water splitting

Photocatalytic hydrogen generation trials were carried out by employing the $Ni@SnO_2$ nanostructures under visible light irradiation in the water splitting reaction facilitated by a 20% aqueous methanol (v/v) solution, and the noteworthy con-clusions are presented in Fig. 15. During the hydrogen evol-ution process, methanol plays dual roles, primarily as a sacrifi-cial reagent to efficiently subdue the oxygen evolution rate, and secondly, participating in an irrevocable reaction with the photogenerated valence band holes from the semiconductor to reduce the rate of charge carrier recombination, which, in turn, assists in the amplification of photocatalytic activity.[76] For the pristine SnO_2 sample, a maximum hydrogen pro-duction of 24 μmol g^{-1} (in 3 h) was found, which was the smal-lest among all the samples (Fig. 15). The hydrogen production rate of $Ni@SnO_2$ nanostructures at lower Ni loading concen-trations were substantially small but exhibited a noteworthy increase with higher loading until the 0.3%$Ni@SnO_2$ nano-structure sample. Above 0.3% Ni loading, a steady decline in


Fig. 15 Photocatalytic hydrogen generation rates of the prepared pris-tine SnO_2 and $Ni@SnO_2$ nanostructures.

the hydrogen production was noted. The hydrogen generation data for all samples are summarized in Table 1, and the highest hydrogen evolution rate was detected for the 0.3% $Ni@SnO_2$ nanostructure with a value of 49.9 μmol h^{-1} g^{-1}, which is ~6 times higher than that for the pristine SnO_2 sample. The achieved photocatalytic water splitting value for the 0.3%$Ni@SnO_2$ nanostructure was found to be on par with reported values, as presented in Table 5. It may be noted that most of the reports presented in Table 5 deal with the doping of SnO_2 with different materials. However, doping may not be an efficient process, due to the non-uniform distribution of dopants. Additionally, there are a few reports on the use of noble metals such as platinum on the SnO_2 surface, which makes the process uneconomical.

This increase in the photocatalytic performance can be attributed to the loading with Ni, an efficient noble metal (Pt)-free co-catalyst, effecting swift and effortless charge separation for surface-activated SnO_2 semiconductor nanoparticle bands. It may be noted that Ni not only acts as a co-catalyst, but also interacts electronically, as inferred from Raman, UV-visible

Fig. 14 *C–V* measurement of pristine SnO_2 and 0.3% $Ni@SnO_2$ samples.

Table 5 Comparison of photocatalytic performance of $Ni@SnO_2$ nano-structures with reported SnO_2 composites

Sr. No.	SnO_2-based Material	H_2 generation yield μmol g^{-1} h^{-1}	Ref.
1.	Boron-doped SnO_2	63.6184	70
2.	Carbon-doped SnO_2	38.43	82
3.	N-doped SnO_2	42.5	83
4.	Pt/Ni(OH)$_2$$SnO_2$	0.9	26
	Pt/Ni(OH)$_2$–Ni$_2$O$_3$–SnO_2	10.8	
5.	Ce–doped SnO_2 nanoparticles	25	84
6.	ZnO–SnO_2 thin films	14 (μmol h^{-1})	85
7.	BiVO$_4$ quantum dot decorated screw-like SnO_2 nanostructures	1.16 (μmol h^{-1} cm^{-2})	86
8.	0.3% $Ni@SnO_2$	49.98	Present work

and PL spectroscopic data, probably creating directional charge transfer channels.[77] The strong electronic interface between Ni-related surface states (playing a role similar to a dopant) and the SnO_2 matrix material states through these channels affects the surface acceptor states, with ensuing negative charge at the semiconductor surface.[51]

The photocatalytic water splitting mechanism comprises sunlight absorption by semiconductor photocatalysts (SnO_2) transferring electrons from the valence band (VB) to the conduction band (CB), leaving behind holes in the VB. These holes produce protons (H^+) and radicals *via* the oxidization of methanol.[78] Simultaneously, generation of molecular hydrogen by the reduction of protons through the electrons of the CB occurs by means of a sequence of reactions.[79] However, this process occurs if rapid recombination of electrons and holes is retarded. In case of the pristine SnO_2 sample, the observed low H_2 production is attributable to the rapid recombination of such photogenerated charges. In the case of the Ni@SnO_2 nanostructures, the significant enhancement in the hydrogen evolution with varying nickel loading concentrations in SnO_2 can be ascribed to several aspects. Initially, the increase in nickel loading from 0.1% to 0.3% enhanced the density of active sites available on the surface of the SnO_2 nanoparticles, which facilitated effective hydrogen evolution reaction (HER). Additionally, nickel acts as a co-catalyst for the HER due to its ability to adsorb hydrogen atoms and enable their combination to form hydrogen molecules, eliminating the need for the expensive Pt co-catalyst. At lower Ni loading concentrations, the presence of nickel enhances the catalytic activity of the SnO_2 surface, promoting the HER. However, beyond 0.3% Ni loading, excessive nickel may result in the formation of inactive nickel clusters causing catalytic poisoning, leading to a decline in the catalytic activity and consequently, in the hydrogen evolution rate.

Noble metals such as Au, Ag, Pt, *etc.*, have been reported to alter the electron distribution to improve SnO_2-based photocatalytic H_2 production.[24] The conduction band level of the target matrix SnO_2 (−0.42 eV), is higher than that of Ni (−0.23 eV) above the H_2 evolution potentials, forming a Schottky barrier at the contact interface. Electrons drift from the high energy levels of SnO_2 to Ni, which acts as an electron acceptor, confining the electrons, which in turn averts photogenerated charge carrier recombination.[80,81] Consequently, the efficiency of photocatalytic H_2 production by autocatalytically deposited Ni on the SnO_2 photocatalyst surface was found to be greatly enhanced.[24]

It is worth noting that the obtained photocatalytic hydrogen production data was substantiated by the PL spectroscopy and BET results. In the PL results, the intensity of peaks corresponding to near-band-edge UV emission (364 nm) and defects (468 nm) were quenched due to generation of a non-radiative epicentre (Fig. 6). Additionally, the BET surface area increased until the Ni loading reached 0.3% and then decreased for the Ni@SnO_2 nanostructures. Both these effects eventually affected the photocatalytic hydrogen production. CV data provided substantial evidence that Ni loading enhanced the charge capacitance of SnO_2, indicating better electrochemical performance. However, further optimization is needed to achieve efficient solar hydrogen production.

Conclusion

A hitherto unreported Ni@SnO_2 photocatalytic system active under visible light was prepared by the co-precipitation synthesis of SnO_2 nanoparticles followed by autocatalytic Ni loading. The nickel loading was varied from 0.1 to 0.5 wt% on surface-activated SnO_2 nanopowders. Ni was uniformly deposited as nanoparticles and surface coating onto the SnO_2 nanopowder surface, as confirmed by FETEM equipped with EDS as well as XPS spectroscopy. The Ni^{2+} loading on the SnO_2 nanopowder surface quenched the PL peak intensity and modified the defect band structure, leading to efficient photogenerated charge carrier separation. The significant improvement in photocatalytic H_2 production for the Ni@SnO_2 nanostructures compared to the pristine SnO_2 nanoparticles could be ascribable to Schottky barrier formation between SnO_2 to Ni and subsequent transfer of photogenerated electrons from the semiconductor to the metal. A maximum hydrogen generation of ~50 $\mu mol\ g^{-1}\ h^{-1}$ was recorded for the 0.3%Ni@SnO_2 nanopowder, which was almost ~6 greater more than the 8.52 $\mu mol\ g^{-1}\ h^{-1}$ obtained for the pristine SnO_2 nanopowder. The present work highlights the efficacy of the autocatalytic deposition technique in producing a hitherto unreported effective and economical Ni@SnO_2-nanostructure-based heterogeneous photocatalyst. We optimistically believe that the autocatalytic deposition technique elaborated in the present study will represent an innovative pathway for surface decoration of exceedingly competent heterogeneous photocatalytic systems for semiconductor materials.

Author contributions

The experiments have been planned & performed by P. N. B. under the supervision of B. K., who introduced the idea of electroless Ni plating. S. R., R. C. and S. G. have supported the characterization. The data were analysed by P. N. B., M. S. and S. A. All the authors have participated in writing the manuscript.

Data availability

Data will be made available on request.

Conflicts of interest

There are no conflicts to declare.

Acknowledgements

References

1 S. Bagheri and N. M. Julkapli, *Int. J. Hydrogen Energy*, 2020, **45**, 31538–31554.

2 C. Wang and D. Astruc, *Chem. Soc. Rev.*, 2021, **50**, 3437–3484.

3 F. Nadeem, H. Zhang, N. Tahir, Z. Zhang, R. R. Singhania, M. Shahzaib, H. Ramzan, M. Usman, M. Rahman and Q. Zhang, *Bioresour. Technol.*, 2023, **382**, 129221.

4 N. Bion, D. Duprez and F. Epron, *ChemSusChem*, 2012, **5**, 76–84.

5 Y. Mao, Y. Gao, W. Dong, H. Wu, Z. Song, X. Zhao, J. Sun and W. Wang, *Appl. Energy*, 2020, **267**, 114860.

6 X. Zhang, M. Shakeel, B. Li and L. Wang, *Electrochim. Acta*, 2020, **331**, 135369.

7 N. Fajrina and M. Tahir, *Int. J. Hydrogen Energy*, 2019, **44**, 540–577.

8 L. C. Goveas, S. Nayak, R. Vinayagam, R. Selvaraj and A. Pugazhendhi, *Fuel*, 2023, **348**, 128460.

9 S. Sahani, K. M. Tripathi, T. I. Lee, D. P. Dubal, C.-P. Wong, Y. C. Sharma and T. Y. Kim, *Energy Convers. Manage.*, 2022, **252**, 115133.

10 B. Guan, J. Yu, S. Guo, S. Yu and S. Han, *Nanoscale Adv.*, 2020, **2**, 1352–1357.

11 J. Kegel, I. M. Povey and M. E. Pemble, *Nano Energy*, 2018, **54**, 409–428.

12 M. B. Costa, M. A. de Araújo, M. V. D. L. Tinoco, J. F. D. Brito and L. H. Mascaro, *J. Energy Chem.*, 2022, **73**, 88–113.

13 C. M. Suarez, S. Hernández and N. Russo, *Appl. Catal., A*, 2015, **504**, 158–170.

14 S. H. Chen, Y. S. Jiang and H. Y. Lin, *ACS Omega*, 2020, **5**, 8927–8933.

15 X. Zheng, L. Feng, Y. Dou, H. Guo, Y. Liang, G. Li, J. He, P. Liu and J. He, *ACS Nano*, 2021, **15**, 13209–13219.

16 S. Wu, J. Sun, Q. Li, Z. D. Hood, S. Yang, T. Su, R. Peng, Z. Wu, W. Sun, P. R. C. Kent, B. Jiang and M. F. Chisholm, *ACS Appl. Mater. Interfaces*, 2020, **12**, 20067–20074.

17 J. Yadav, P. Raturi, S. Yadav and J. P. Singh, *Renewable Energy*, 2021, **179**, 2256–2266.

18 V. Hasija, P. Raizada, A. Hosseini-Bandegharaei, V. K. Thakur, Q. Van Le, V. H. Nguyen and P. Singh, *ChemCatChem*, 2021, **13**, 2965–2987.

19 Y. Xu, D. Li, Q. Zeng, H. Sun and P. Li, *RSC Adv.*, 2023, **13**, 27676–27685.

20 A. Chauhan, Sonu, P. Raizada, P. Singh, T. Ahamad, V.-H. Nguyen, Q. V. Le, A. A. P. Khan, N. Kumar, A. Sudhaik and C. M. Hussain, *J. Ind. Eng. Chem.*, 2024, **130**, 25–53.

21 J. A. Nasir, Z. U. Rehman, S. N. A. Shah, A. Khan, I. S. Butler and C. R. A. Catlow, *J. Mater. Chem. A*, 2020, **8**, 20752–20780.

22 S. Singh and S. K. Kansal, *Appl. Mater. Today*, 2022, **26**, 101345.

23 H. Luo, Z. Zeng, G. Zeng, C. Zhang, R. Xiao, D. Huang, C. Lai, M. Cheng, W. Wang, W. Xiong, Y. Yang, L. Qin, C. Zhou, H. Wang, Y. Zhou and S. Tian, *Chem. Eng. J.*, 2020, **383**, 123196.

24 C. Sun, J. Yang, M. Xu, Y. Cui, W. Ren, J. Zhang, H. Zhao and B. Liang, *Chem. Eng. J.*, 2022, **427**, 131564.

25 S. Das and V. Jayaraman, *Prog. Mater. Sci.*, 2014, **66**, 112–255.

26 Q. Du and G. Lu, *Appl. Surf. Sci.*, 2014, **305**, 235–241.

27 Y. Y. Li, B. X. Zhou, H. W. Zhang, S. F. Ma, W. Q. Huang, W. Peng, W. Hu and G. F. Huang, *Nanoscale*, 2019, **11**, 6876–6885.

28 Y.-Y. Li, B.-X. Zhou, H.-W. Zhang, T. Huang, Y.-M. Wang, W.-Q. Huang, W. Hu, A. Pan, X. Fan and G.-F. Huang, *Chem. Eng. J.*, 2022, **430**, 132880.

29 A. Mamakhel, M. Søndergaard, K. Borup and B. B. Iversen, *J. Supercrit. Fluids*, 2020, **166**, 105029.

30 S. Naz, I. Javid, S. Konwar, K. Surana, P. K. Singh, M. Sahni and B. Bhattacharya, *SN Appl. Sci.*, 2020, **2**, 2–9.

31 G. H. Patel, S. H. Chaki, R. M. Kannaujiya, Z. R. Parekh, A. B. Hirpara, A. J. Khimani and M. P. Deshpande.

32 S. Das, K. G. Girija, A. K. Debnath and R. K. Vatsa, *J. Alloys Compd.*, 2021, **854**, 157276.

33 N. Nabihah-Fauzi, N. Asikin-Mijan, M. L. Ibrahim, H. Hashim, S. Yusup, Y. H. Taufiq-Yap and M. S. Mastuli, *RSC Adv.*, 2020, **10**, 29187–29201.

34 J. Liu, K. Kempa and J. Gao.

35 R. B. Rajput and R. B. Kale, *Environ. Adv.*, 2021, **5**, 100081.

36 I. Ullah, A. Munir, S. Muhammad, S. Ali, N. Khalid, M. Sirajuddin, S. Z. Hussain, S. Ahmed, Y. Khan, I. Hussain, A. Haider, A. Munir, S. Muhammad, S. Ali, N. Khalid, M. Zubair, M. Sirajuddin, S. Z. Hussain, S. Ahmed, Y. Khan, I. Hussain and A. Haider, *J. Alloys Compd.*, 2020, **827**, 154247.

37 Y. C. Chang, C. Y. Yan and R. J. Wu, *J. Chin. Chem. Soc.*, 2014, **61**, 345–349.

38 I. Marić, G. Dražić, E. Radin, R. Peter, M. Škrabić, T. Jurkin, A. Pustak, N. Baran, L. Mikac, M. Ivanda, M. Petravić, G. Štefanić and M. Gotić, *Appl. Surf. Sci.*, 2023, **607**, 155073.

39 Y. Sun, Q. Zhu, B. Bai, Y. Li and C. He, *Chem. Eng. J.*, 2020, **390**, 124518.

40 H. Wang, K. Zhang, J. Qiu, J. Wu, J. Shao, Y. Deng, Y. Wu and L. Yan, *Energy Fuels*, 2021, **35**, 12516–12526.

41 Y. Ye, Y. Wang, Z. Li, Y. Ye, Y. Liu, X. Zou and S. Lin, *New J. Chem.*, 2019, **43**, 17023–17032.

42 G. O. Testoni, R. A. C. Amoresi, G. M. M. Lustosa, J. P. C. Costa, M. V. Nogueira, M. Ruiz, M. A. Zaghete and L. A. Perazolli, *Solid State Sci.*, 2018, **76**, 65–73.

43 S. Jana, S. Konar, B. C. Mitra, A. Mondal and S. Mukhopadhyay, *Mater. Res. Bull.*, 2021, **141**, 111351.

44 V. S. Suvith, V. S. Devu and D. Philip, *Ceram. Int.*, 2020, **46**, 786–794.

45 W. Zhang, Y. Yu, R. Huang and X. Shi, *ACS Appl. Mater. Interfaces*, 2021, **13**, 40571–40581.

46 T. Qiu and P. K. Chu, *Mater. Sci. Eng., R*, 2008, **61**, 59–77.

47 Ş. Neaţu, F. Neaţu, V. C. Diculescu, M. M. Trandafir, N. Petrea, S. Somacescu, F. Krumeich, J. T. C. Wennmacher, A. J. Knorpp, J. A. Van Bokhoven and M. Florea, *ACS Appl. Mater. Interfaces*, 2020, **12**, 18407–18420.

48 P. N. Birla, S. Arbuj, M. D. Shinde, S. Joseph, S. Rane, S. Kulkarni and B. Kale, *RSC Adv.*, 2023, **13**, 20068–20080.

49 T. Boettcher, S. Schaefer, M. Antoni, T. Stohr, U. Kunz, M. Dürrschnabel, L. Molina-Luna, W. Ensinger and F. Muench, *Langmuir*, 2019, **35**, 4246–4253.

50 F. Muench, *ChemElectroChem*, 2021, **8**, 2993–3012.

51 K.-I. Choi, M. Hübner, A. Haensch, H.-J. Kim, U. Weimar, N. Barsan and J.-H. Lee, *Sens. Actuators, B*, 2013, **183**, 401–410.

52 M. Kandasamy, A. Seetharaman, D. Sivasubramanian, A. Nithya, K. Jothivenkatachalam, N. Maheswari, M. Gopalan, S. Dillibabu and A. Eftekhari, *ACS Appl. Nano Mater.*, 2018, **1**, 5823–5836.

53 K. K. Supin, A. George, Y. R. Kumar, K. K. Thejas, G. Mandal, A. Chanda and M. Vasundhara, *RSC Adv.*, 2022, **12**, 26712–26726.

54 A. Mohammad, M. E. Khan, M. R. Karim, M. H. Cho and T. Yoon, *Ceram. Int.*, 2021, **47**, 23578–23589.

55 L. M. Jose, N. S. George, S. A. Kadam, S. Athira, A. Kripa, A. Aravind, Y.-R. Ma and Y.-R. Chen, *Opt. Mater.*, 2023, **135**, 113348.

56 X. Wei, C. Wan, Y. Zhang, Q. Zhong and H. Qu, *Int. J. Hydrogen Energy*, 2023, **48**, 36403–36411.

57 L. Fan, P. F. Liu, X. Yan, L. Gu, Z. Z. Yang, H. G. Yang, S. Qiu and X. Yao, *Nat. Commun.*, 2016, **7**, 1–7.

58 F. H. Aragón, J. A. H. Coaquira, P. Hidalgo, S. W. Da Silva, S. L. M. Brito, D. Gouvêa and P. C. Morais, *J. Raman Spectrosc.*, 2011, **42**, 1081–1086.

59 A. Diéguez, A. Romano-Rodríguez, A. Vilà and J. R. Morante, *J. Appl. Phys.*, 2001, **90**, 1550–1557.

60 I. M. Costa, Y. N. Colmenares, P. S. Pizani, E. R. Leite and A. J. Chiquito, *Chem. Phys. Lett.*, 2018, **695**, 125–130.

61 L. Ying-Kai, D. Yi and W. Guang-Hou, *Chin. Phys. Lett.*, 2004, **21**, 156.

62 Y. Fu, J. Li and H. Xu, *Mater. Sci. Semicond. Process.*, 2020, **114**, 105073.

63 S. Mehraj, M. S. Ansari and Alimuddin, *Thin Solid Films*, 2015, **589**, 57–65.

64 N. Bhardwaj, B. Satpati and S. Mohapatra, *Appl. Surf. Sci.*, 2020, **504**, 144381.

65 P. Chetri and A. Choudhury, *Phys. E*, 2013, **47**, 257–263.

66 A. G. Habte, F. G. Hone and F. B. Dejene, *Physica B: Condens. Matter*, 2020, **580**, 411832.

67 J. Park, S. S. Lam, Y.-K. Park, B.-J. Kim, K.-H. An and S.-C. Jung, *Environ. Res.*, 2023, **216**, 114657.

68 S. Sen, S. Maity and S. Kundu, *J. Alloys Compd.*, 2023, **966**, 171553.

69 P. Renganathan, S. Marimuthu, R. Kanniah, V. Karthikeyan and G. A. Sundaram, *Results Chem.*, 2022, **4**, 100557.

70 S. Kumar, Bhawna, S. K. Yadav, A. Gupta, R. Kumar, J. Ahmed, M. Chaudhary, Suhas and V. Kumar, *Environ. Sci. Pollut. Res.*, 2022, **29**, 47448–47461.

71 D. Chen, S. Huang, R. Huang, Q. Zhang, T. T. Le, E. Cheng, R. Yue, Z. Hu and Z. Chen, *J. Hazard. Mater.*, 2019, **368**, 204–213.

72 B. Lei, H. Zhang, W. Liu, Q. Zhao, Y. Wei, Y. Lu, X. Yang, W. Zhang, T. Xiao, J. Kong and W. Cai, *Sens. Actuators, B*, 2024, **401**, 134907.

73 J. Shi, N. Lin, D. Liu, Y. Wang and H. Lin, *J. Electroanal. Chem.*, 2020, **857**, 113634.

74 L. Sang, G. Xu, Z. Chen, X. Wang, H. Cui, G. Zhang and Y. Dou, *Mater. Sci. Semicond. Process.*, 2020, **105**, 104710.

75 N. O. Laschuk, E. B. Easton and O. V. Zenkina, *RSC Adv.*, 2021, **11**, 27925–27936.

76 K. Sathiyan, R. Bar-Ziv, V. Marks, D. Meyerstein and T. Zidki, *Chem. – Eur. J.*, 2021, **27**, 15936–15943.

77 B. Li, Z. Tian, L. Li, Y. H. Wang, Y. Si, H. Wan, J. Shi, G. F. Huang, W. Hu, A. Pan and W. Q. Huang, *ACS Nano*, 2023, **17**, 3465–3482.

78 J. Zhao, R. Shi, Z. Li, C. Zhou and T. Zhang, *Nano Sel.*, 2020, **1**, 12–29.

79 Y. Zhang, Y. Dai, H. Li, L. Yin and M. R. Hoffmann, *Commun. Mater.*, 2020, **1**, 1–9.

80 L. Yang, J. Huang, L. Shi, L. Cao, W. Zhou, K. Chang, X. Meng, G. Liu, Y. Jie and J. Ye, *Nano Energy*, 2017, **36**, 331–340.

81 Y. Y. Li, J. G. Wang, H. H. Sun, W. Hua and X. R. Liu, *Int. J. Hydrogen Energy*, 2018, **43**, 14121–14129.

82 K. Mallikarjuna, G. A. K. M. Rafiqul Bari, S. V. P. Vattikuti and H. Kim, *Int. J. Hydrogen Energy*, 2020, **45**, 32789–32796.

83 Bhawna, A. Gupta, P. Kumar, A. Tyagi, R. Kumar, A. Kumar, P. Singh, R. P. Singh and V. Kumar, *ChemistrySelect*, 2020, **5**, 7775–7782.

84 V. Kumar, Bhawna, S. K. Yadav, A. Gupta, B. Dwivedi, A. Kumar, P. Singh and K. Deori, *ChemistrySelect*, 2019, **4**, 3722–3729.

85 A. Saldaña-Ramírez, M. R. A. Cruz, I. Juárez-Ramírez and L. M. Torres-Martínez, *Opt. Mater.*, 2020, **110**, 110501.

86 M. Xie, Z. Zhang, W. Han, X. Cheng, X. Li and E. Xie, *J. Mater. Chem. A*, 2017, **5**, 10338–10346.